JACS Au
AN OPEN ACCESS JOURNAL OF THE AMERICAN CHEMICAL SOCIETY

pubs.acs.org/jacsau
Article

Defect and Donor Manipulated Highly Efficient Electron−Hole Separation in a 3D Nanoporous Schottky Heterojunction

Chunyu Yuan, Hongfei Yin, Huijun Lv, Yujin Zhang, Jing Li, Dongdong Xiao, Xiaoyong Yang, Yongzheng Zhang,* and Ping Zhang

Cite This: JACS Au 2023, 3, 3127−3140

Read Online

ACCESS | Metrics & More | Article Recommendations | Supporting Information

ABSTRACT: Given the rapid recombination of photogenerated charge carriers and photocorrosion, transition metal sulfide photocatalysts usually suffer from modest photocatalytic performance. Herein, S-vacancy-rich $ZnIn_2S_4$ (V_S-ZIS) nanosheets are integrated on 3D bicontinuous nitrogen-doped nanoporous graphene (N-npG), forming 3D heterostructures with well-fitted geometric configuration (V_S-ZIS/N-npG) for highly efficient photocatalytic hydrogen production. The V_S-ZIS/N-npG presents ultrafast interfacial photogenerated electrons captured by the S vacancies in V_S-ZIS and holes neutralization behaviors by the extra free electrons in N-npG during photocatalysis, which are demonstrated by in situ XPS, femtosecond transient absorption (fs-TA) spectroscopy, and transient-state surface photovoltage (TS-SPV) spectra. The simulated interfacial charge rearrangement behaviors from DFT calculations also verify the separation tendency of photogenerated charge carriers. Thus, the optimized V_S-ZIS/N-npG 3D hierarchical heterojunction with 1.0 wt % N-npG exhibits a comparably high hydrogen generation rate of 4222.4 μmol g^{-1} h^{-1}, which is 5.6-fold higher than the bare V_S-ZIS and 12.7-fold higher than the ZIS without S vacancies. This work sheds light on the rational design of photogenerated carrier transfer paths to facilitate charge separation and provides further hints for the design of hierarchical heterostructure photocatalysts.

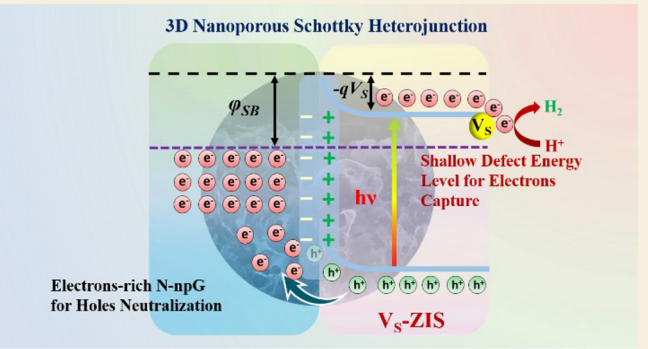

KEYWORDS: *3D heterostructure, electrons capture, holes neutralization, charge separation, photocatalytic hydrogen generation*

INTRODUCTION

Taking advantage of sustainable solar energy efficiently has been intensively pursued by researchers to solve the environmental pollution and energy crisis.[1−3] It is theoretically and practically prospective to produce clean hydrogen fuel by cost-effective photocatalytic water splitting. Transition metal sulfide photocatalysts hold excellent visible-light absorption capacity benefiting from narrow bandgap and applicable thermodynamic band position for photocatalytic hydrogen evolution.[4−6] However, the pristine transition metal sulfide photocatalysts are always subject to the rapid recombination of charge carriers and photocorrosion caused by photogenerated holes, which will cause non-negligible impairment to the photocatalytic activity and stability. It is therefore pivotal to take some suitable measures to overcome the photocorrosion and accelerate the separation and migration kinetics of photogenerated charge carriers. S vacancies, the strong electron-withdrawing groups originating from the discrete defect energy levels, are generally regarded as active sites during catalysis.[7−9] The introduction of anion S vacancies has been considered an operative defect engineering modulation approach to enhance the separation of charge carriers.[10−13] Nevertheless, the underlying mechanism caused by S vacancies to accelerate photocatalysis is pending further exploration and verification.

3D nanoporous graphene as a new type of catalyst and outstanding guest catalyst not only retains the excellent characteristics of original 2D planar graphene but also possesses a hierarchical network and diverse pore distribution.[14,15] The interconnected nanopore channels and three-dimensional curvature in porous architecture graphene are in favor of the multiple reflection and scattering of the incident light, contributing to the enhanced light absorption and utilization capacity.[16,17] Moreover, the 3D charge transport channels further promote the migration of charge carriers and the diffusion of gas products. Heteroatom doping of graphene has been verified operative to modulate the electronic structure and local electron density distribution, which endows it with great opportunities for diversified applications.[18−22] However,

Received: August 18, 2023
Revised: September 29, 2023
Accepted: October 3, 2023
Published: October 21, 2023

the regulation of the microenvironment of electron distribution tailored by the defects and donors at the heterojunction interface has not yet been explicitly rationalized.

Because $ZnIn_2S_4$ is a typical promising AB_2X_4 family semiconductor with d^{10} electronic configuration, it is also less poisonous in comparison with the typical metal sulfides (e.g., CdS, Sb_2S_3), which enables it to be more pragmatic for application in environmental optimization.[23−25] In this work, $ZnIn_2S_4$ nanosheets with S vacancies (V_S-ZIS) were assembled on N-doped nanoporous graphene (N-npG) to construct three-dimensional (3D) heterostructures for photocatalytic hydrogen evolution. The rationally introduced S vacancy defects in $ZnIn_2S_4$ served as efficient electronic reservoirs to promote the utilization of photogenerated electrons for reducing hydrogen protons efficiently. By doping of an electron-rich N heteroatom for introducing extra electrons without changing the zero bandgap semimetal property of graphene, the provided extra electrons in 3D nanoporous graphene potentially extract and neutralize the photogenerated holes from V_S-$ZnIn_2S_4$ (V_S-ZIS), promoting the separation of photogenerated carriers and holding back the harmful photocorrosion. The Schottky heterojunction formed by zero bandgap N-npG and V_S-ZIS introduces the Schottky barrier including the upward bending valence band of V_S-ZIS, which is to the benefit of hole derivation and recombination with the extra electrons in N-npG. In addition, the 3D nanoporous heterostructure endows the photocatalysts with enhanced light absorption and utilization capacity as well as fully exposed active sites. Owing to efficient interfacial separated states and long-lived shallow trapping of photoelectrons, the 3D heterojunction of V_S-ZIS/N-npG exhibits a significantly improved photocatalytic hydrogen evolution rate and holds excellent stability after a long-term stability test. This work highlights the construction of well-fitted hierarchical heterostructure photocatalysts and the specific design of an electron−hole transfer path to accelerate charge separation for photocatalytic hydrogen production.

EXPERIMENTAL SECTION

Materials

Potassium chloride (KCl), ammonium sulfate ($(NH_4)_2SO_4$) and sodium sulfate (Na_2SO_4) were supplied by Sinopharm Chemical Reagent Co., Ltd. (Shanghai, China). Indium trichloride ($InCl_3·4H_2O$), zinc acetate dihydrate ($Zn(CH_3COO)_2·2H_2O$), thioacetamide (C_2H_5NS), benzene (C_6H_6), pyridine (C_5H_5N), potassium ferricyanide ($K_3[Fe(CN)_6]$) and potassium hexacyanoferrate ($K_4[Fe(CN)_6]$) were purchased from Aladdin Bio-Chem Technology Co., Ltd., Shanghai, China. 2D normal graphene powder was offered by Tanfeng Tech., Inc., Suzhou, China. Hydrochloric acid (HCl) was obtained from Yuandong Fine Chemicals Co., Ltd., Yantai, China.

Preparation of Nanoporous Graphene (npG) and N-doped Nanoporous Graphene (N-npG)

The chemical vapor deposition (CVD) method was applied to prepare the N-doped nanoporous graphene based on the previous reports.[15,26] Nanoporous Ni obtained by dealloying the $Ni_{30}Mn_{70}$ alloy in 1 M $(NH_4)_2SO_4$ was used as the porous substrate for graphene growth. After the preprocessing procedure, the programmed heating device was heated to 850 °C with a speed of 20 °C per minute with 500 sccm Ar/H_2 (5%) gas mixture, and then pyridine preheating to 45 °C was used as the carbon source and conveyed with 2500 sccm Ar/H_2 (5%) for 6 min. After cooling the inner quartz tube to room temperature rapidly with an automatic cooling device, 3D N-doped nanoporous graphene coated on a nanoporous Ni scaffold was obtained. Then 3D free-standing N-doped graphene with a bicontinuous nanoporous structure was prepared by exfoliating the Ni scaffold in 2.0 M hydrochloric acid (HCl) solution and washing in deionized water and ethanol six times with further supercritical drying. Benzene and pyridine were applied as carbon sources to synthesize 3D nanoporous graphene (npG) and N-doped nanoporous graphene (N-npG).

Preparation of $ZnIn_2S_4$, S-Vacancy-Rich $ZnIn_2S_4$ and Composites

The V_S-ZIS/N-npG heterojunction was hydrothermally prepared by anchoring S-vacancy-rich $ZnIn_2S_4$ (V_S-ZIS) nanosheets on 3D N-doped nanoporous graphene (N-npG). Typically, 87.8 mg of zinc acetate dihydrate and 234.6 mg of indium trichloride were dispersed in a 30 mL mixture solution under vigorous stirring for 30 min, in which the volume ratio of deionized water to absolute alcohol is 1:1. Then under slow magnetic stirring at 200 rpm, a certain amount of 3D N-doped nanoporous graphene (N-npG) was added and stirred for 2 h. 240.4 mg of thioacetamide (TAA) was then immersed in the mixture. The as-obtained homogeneous aqueous solution was reacted at 180 °C for 24 h in a 50 mL reaction still. After cooling the sediments to room temperature, the as-prepared products were repeatedly washed with deionized water as well as ethanol and were kept at 70 °C for 6 h under vacuum conditions until dry. Herein, the weight ratios of N-npG to V_S-ZIS was modulated to be 0, 0.5, 1.0, 1.5, and 2.0 wt %, which were labeled as V_S-ZIS, V_S-ZIS/N-npG 0.5, V_S-ZIS/N-npG 1.0, V_S-ZIS/N-npG 1.5 and V_S-ZIS/N-npG 2.0, respectively. In order to synthesize ZIS and ZIS/N-npG 1.0 without S vacancies for contrast, the weight of added TAA was halved when preparing ZIS. Besides, V_S-ZIS/npG 1.0 and V_S-ZIS/2DG 1.0 composites were also prepared for comparison using the nanoporous graphene (npG) and 2D normal graphene (2DG) as supporting matrixes, respectively, at an optimized weight percentage of 1.0 wt %.

Material Characterization

X-ray diffraction (XRD) results were collected on a Rigaku D/Max-cA X-ray diffractometer to obtain the crystalline and phase features with a Ni filter and Cu Kα radiation. Raman spectra were recorded using a Finder One microzone laser Raman spectroscopic system from Beijing Zolix, Ltd., with an incident wavelength of 532 nm. The morphological images were observed on a scanning electron microscope (SEM) (Carl Zeiss Ultra 55, 5 kV). TEM and HRTEM images as well as the corresponding EDS spectra were obtained on a field-emission transmission electron microscope (TEM) (JEOL JEM-2100F, 200 kV). X-ray photoelectron spectroscopy (XPS) including in situ XPS measurements and ultraviolet photoelectron spectroscopy (UPS) measurements were conducted on an AXIS Supra+ spectrometer with monochromatized Al Kα excitation and He I radiation. A clean Au sample with the Au $4f_{7/2}$ at 84.0 eV was applied for XPS calibration. The size distribution and specific surface area were determined by the Brunauer−Emmett−Teller (BET) nitrogen adsorption−desorption techniques with an automated surface area and porosity analyzer (ASAP 2460, Micromeritics, U.S.A.). The samples were pretreated at 120 °C before the BET tests. Electron paramagnetic resonance (EPR) (JESFA200, JEOL Co., Japan) was employed to detect the presence and behavior of the native defects. With $BaSO_4$ as a reference, the optical absorption spectra were monitored on a Lambda 1050 spectrophotometer (PerkinElmer) within the scope of 300−800 nm. Photoluminescence (PL) and time-resolved photoluminescence (TRPL) spectra were measured by a fluorescent spectrometer (Edinburgh, FLS1000, 400 nm excitation). Transient-state SPV (TS-SPV) spectra were conducted on a CEL-TPV 2000 instrument with a laser wavelength of 355 nm. The experimental details of in situ XPS, femtosecond transient absorption (fs-TA) spectroscopy and photoelectrochemical measurements details are described in the Supporting Information.

Photocatalytic Hydrogen Generation Performance Measurements

The photocatalytic hydrogen evolution performance tests were conducted in a Pyrex flask with a total volume of 215 mL. In a 40 mL mixed aqueous solution involving Na_2S (0.25 M)/Na_2SO_3 (0.35

https://doi.org/10.1021/jacsau.3c00482
JACS Au 2023, 3, 3127−3140

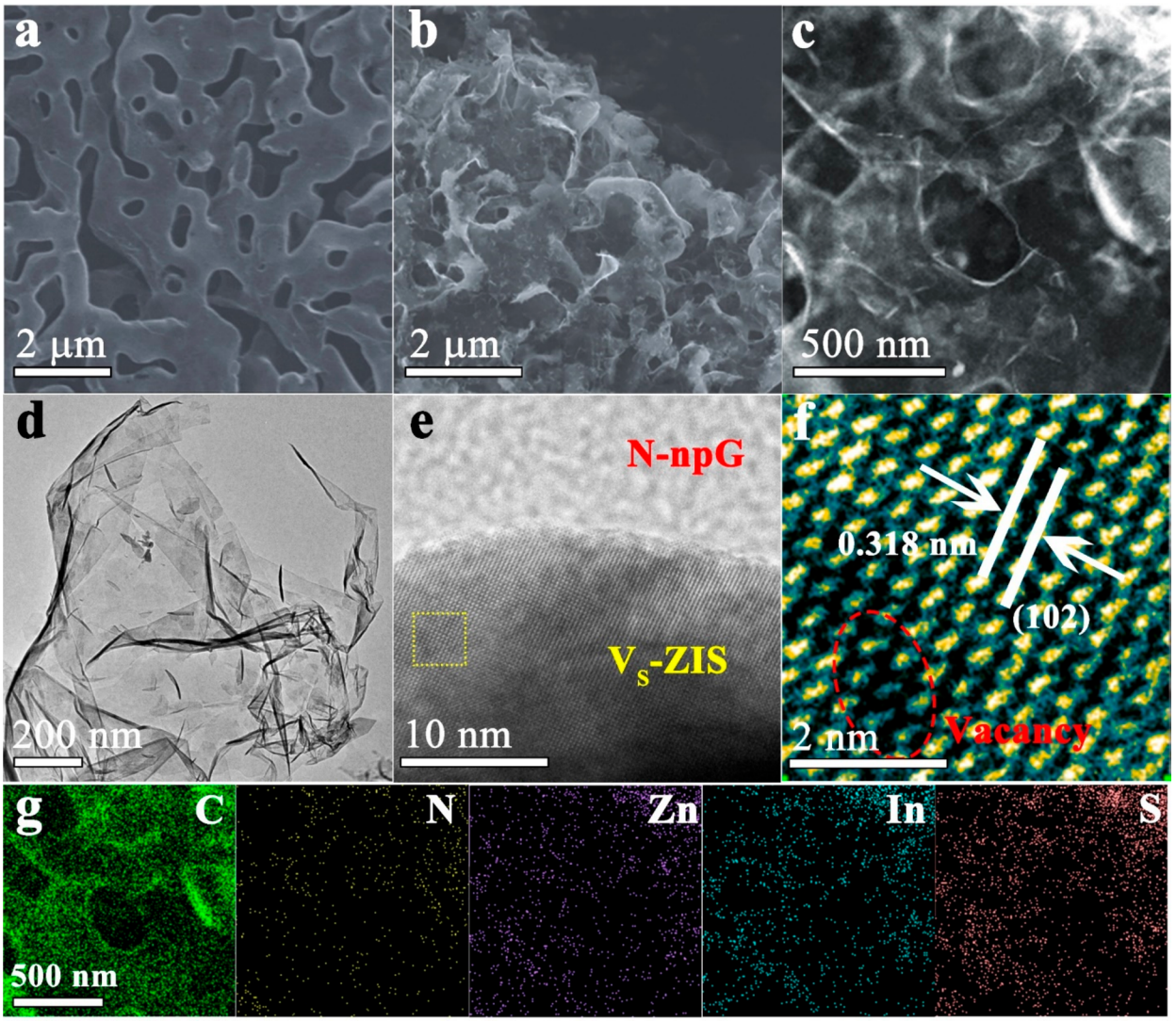

Figure 1. SEM images of (a) N-npG and (b) V_S-ZIS/N-npG. (c–f) HAADF-STEM and HRTEM images of V_S-ZIS/N-npG. (g) Corresponding elemental distributions of C, N, Zn, In and S over V_S-ZIS/N-npG.

M) as hole sacrificial agents, 20 mg of the as-prepared samples was immersed for the photocatalytic hydrogen generation reaction. Before illumination, the cyclic photochemical temperature control integrated reactor was installed in the online integrated photocatalytic activity evaluation system (CEL-PAEM-D8Pro) equipped with a CEL-HXF300-T3 300 W xenon lamp source (420 nm < λ < 760 nm). The light intensity is 100 mW/cm^2, which was measured by a thermopile sensor (Newport, model 818P-01-12), and the irradiation spectrum was controlled by the 420 nm cutoff filter as a visible-light source and fixed 12 cm above the solution interface to control the light intensity. The glass system with the reactor is integrated into a closed and shaded box. The glass joint position was sealed with vacuum grease (Dow Corning HVG, U.S.A.). The glass system with the reaction cell was stirred and vacuumed for 20 min before the test to ensure the airtightness of the system. In the process of photocatalysis under continuous stirring, the cooling water circulation equipment was controlled at 6 °C. The generated gas was analyzed with batch scripts every half hour by online gas chromatography (GC-2014, Shimadzu, Japan) equipped with a thermal conductivity detector and argon as carrier.

RESULTS AND DISCUSSION

Materials Characterizations

The topography morphologies and microstructures of V_S-ZIS, N-npG and V_S-ZIS/N-npG were investigated by SEM and TEM, as displayed in Figure 1 and Figure S1. It could be observed in Figure S1a that bare V_S-ZIS presents homogeneously distributed flower-like microspheres with a diameter of 5–6 μm, which are self-assembled by numerous nanosheets, while the TEM image in Figure S1b demonstrates a typical 2D stacked nanosheet structure of $ZnIn_2S_4$. As manifested in Figure 1a and Figure S2, N-npG displays a charming 3D hierarchical bicontinuous nanoporous structure with abundant open nanopore channels. With regard to the V_S-ZIS/N-npG sample, both nanosheet structured V_S-ZIS and 3D porous structured N-npG could be observed in Figure 1b. V_S-ZIS nanosheets are arranged on the surface as well as the pore channel of N-npG, owing to a well-fitted geometric configuration and suitable aperture size of N-npG. The high-resolution observations in Figure 1c–e show that V_S-ZIS nanosheets are attached tightly to the curvature aperture of three-dimensional N-npG. Apparent lattice fringes are detected

https://doi.org/10.1021/jacsau.3c00482
JACS Au 2023, 3, 3127–3140

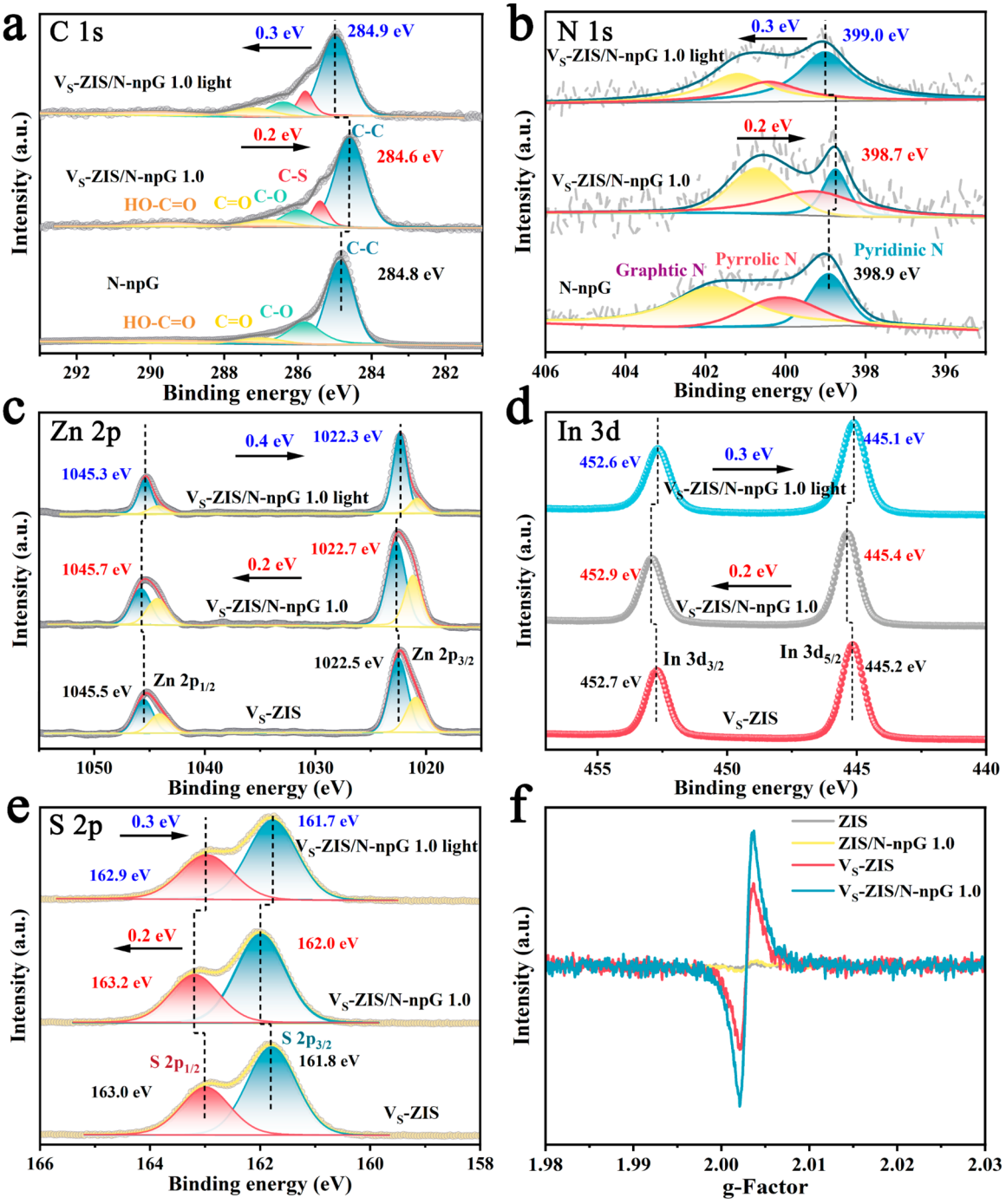

Figure 2. High-resolution in situ XPS spectra for (a) C 1s, (b) N 1s, (c) Zn 2p, (d) In 3d, and (e) S 2p core levels of N-npG, V_S-ZIS and V_S-ZIS/N-npG 1.0 with and without irradiation. (f) EPR spectra of ZIS, ZIS/N-npG 1.0, V_S-ZIS and V_S-ZIS/N-npG 1.0.

in Figure 1f, which is zoomed in the yellow frame in Figure 1e, and the interplanar crystal spacing of 0.318 nm corresponds to the (102) crystal facet of the V_S-ZIS. Noteworthily, some indistinct lattice fringes are detected in the red circles in Figure 1f, due to the existence of vacancy defects in $ZnIn_2S_4$. As verified and discussed below through room-temperature EPR and XPS, the defects that occurred are attributed to the presence of S vacancies. Additionally, the corresponding elemental mappings of V_S-ZIS/N-npG are illustrated in Figure 1g, revealing the uniform distribution of C, N, Zn, In and S elements in the heterostructure material. This favorable 3D heterostructure avoids the adverse aggregation of V_S-ZIS effectively and is conducive to full exposure of reactive sites, which are expected to facilitate the migration of electron−hole pairs between the V_S-ZIS nanosheets and N-npG.

X-ray diffraction (XRD) measurements were applied for investigating the crystalline structure of the as-fabricated samples, as illustrated in Figure S3. The diffraction peaks of V_S-ZIS at 21.6°, 27.8°, 30.5°, 39.7°, 47.4° and 52.4° could be indexed to (006), (102), (104), (108), (110) and (116) crystal facets of the hexagonal phase $ZnIn_2S_4$ (JCPDS 72-0773), respectively.[7,17] 3D N-doped nanoporous graphene displays one characteristic diffraction peak at 2θ = 26.2° coinciding with the (002) crystal plane.[26] Typical V_S-ZIS/graphene

https://doi.org/10.1021/jacsau.3c00482
JACS Au 2023, 3, 3127−3140

heterojunctions demonstrate similar XRD patterns in comparison with the V_S-ZIS, which is primarily on account of the comparatively low percentage composition of graphene.[27] The existence and structural characteristics of the as-prepared graphene supporting matrix were also investigated by Raman measurement (Figure S4). Compared to npG (I_D/I_G = 0.26) and 2DG (I_D/I_G = 0.12), the N-npG (I_D/I_G = 0.33) and V_S-ZIS/N-npG 1.0 (I_D/I_G = 0.41) possess a fairly higher topological defect degree originating from the successful nitrogen doping and thermal treatment.[14,15,28]

To further determine the chemical composition and specific intermolecular interaction in the as-formed heterostructure, the chemical binding states of V_S-ZIS, N-npG, and V_S-ZIS/N-npG 1.0 were determined by in situ X-ray photoelectron spectroscopy (XPS). For rigorous binding energy data, the calibration of XPS peaks was performed concerning the binding energy of Au $4f_{7/2}$ (84.0 eV).[29,30] The existence of Zn, In and S, C and N elements is revealed by the survey XPS spectra of V_S-ZIS and N-npG (Figure S5a), and all signals were observed in the as-prepared V_S-ZIS/N-npG heterojunction. Intimate heterojunction interface contact ensures the highly efficient migration and separation capacity of photogenerated electrons and holes. Four peaks at 284.8, 285.9, 287.0 and 289.9 eV are deconvolved from the C 1s core-level spectra of N-npG in Figure 2a, originating from C—C, C—O, C═O and O═C—OH bonding in the sp^2 hybridization carbon, respectively.[31] However, a supererogatory deconvolved peak of C 1s spectra is observed in V_S-ZIS/N-npG 1.0, which could be attributed to the C−S cross-linked bond.[32] The detected C−S bonds provide a shred of important evidence for the strong interfacial interactions between V_S-ZIS and N-npG. As presented in Figure 2b, the N 1s spectra of N-npG demonstrate the existence of diversiform nitrogen specimens including pyridinic N (398.9 eV), pyrrolic N (400.1 eV) and graphitic N (401.9 eV);[33,34] the total content is about 2.74 at. %.

For the Zn 2p core levels of V_S-ZIS in Figure 2c, characteristic doublets of Zn $2p_{3/2}$ and Zn $2p_{1/2}$ located at 1022.5 and 1045.5 eV correspond to the Zn^{2+} states of $ZnIn_2S_4$. The minor prepeaks centered at lower binding energy including 1020.6 and 1043.7 eV originate from unsaturated coordination of zinc (Zn) by virtue of the existence of S vacancies.[35−37] Similar prepeaks are also observed in the V_S-ZIS/N-npG heterostructure. The presence of incomplete uncoordinated $Zn^{\delta+}$ ($0 < \delta < 2$) atoms around the S vacancies reduces the binding energy of Zn^{2+}. As a result of the smaller defect formation energy of S and weaker electronegativity of Zn, S atoms adjacent to the Zn atom will escape primarily due to the smallest atomic escape energy, and therefore sulfur vacancies adjacent to the Zn atom are formed preferentially.[11,38] In a detail from Figure 2c−e, upon coupling V_S-ZIS with N-npG to form the heterojunction, the binding energies of Zn 2p, In 3d and S 2p are slightly positive shifted by 0.2 eV, which can be attributed to the strong interaction and upward band bending of V_S-ZIS at the interface of V_S-ZIS and N-npG. As a result of the difference in Fermi energy level, electrons are diffused from the V_S-ZIS region to the N-npG region after intimate contact spontaneously until equilibrium; the density of the electron cloud at the surface of V_S-ZIS is thus decreased.[39]

Moreover, XPS tests under light irradiation were also carried out to uncover relative kinetics behaviors of photogenerated carriers in the V_S-ZIS/N-npG system. Notably, the dramatic positive shift of N 1s core levels under irradiation represents the decreased local electron cloud density, demonstrating that N-npG owns a certain electron-donating ability. Thus, it can be deduced that electron-rich N-npG acts as a capturer of photogenerated holes and compensates for the loss of electrons in the valence band of V_S-ZIS upon light excitation. The formation of the Schottky barrier including the upward bending valence band of V_S-ZIS is to the benefit of hole derivation and recombination with the extra electrons in N-npG. The shifts to the lower binding energy of Zn 2p, In 3d and S 2p are observed under light illumination in comparison with V_S-ZIS/N-npG under dark conditions, indicating the strong electron-trapping ability of S vacancies in V_S-ZIS. Besides, the content of incomplete uncoordinated $Zn^{\delta+}$ ($0 < \delta < 2$) is decreased under irradiation (Figure 2c), which could be attributed to the introduced vacancies serving as electron accumulation centers. Photogenerated electrons are more inclined to be trapped by S vacancies on account of the presence of the Schottky barrier including the upward bending conduction band of V_S-ZIS. In Figure S5b, the ultraviolet photoelectron spectroscopy (UPS) technique was applied to elucidate the effect of nitrogen dopants on the electronic structure of graphene. A smaller work function (Φ) of N-npG (4.07 eV) indicates a fairly strong escape ability of electrons compared to that of undoped npG (4.39 eV). Restrained electrons inside N-npG are more easily motivated from the inside N-npG and therefore could combine with photoinduced holes generated from the valence band of V_S-ZIS.

Furthermore, as an effective and intuitive approach to investigate the native defects, room-temperature EPR measurement was also conducted to ensure the introduction of S vacancies. We also prepared comparison samples of ZIS and ZIS/N-npG without sulfur vacancies in order to explore the characteristics of sulfur vacancy. As displayed in Figure 2f, symmetrical EPR signals are detected both in V_S-ZIS and V_S-ZIS/N-npG samples at 3503 G (corresponding to a g-value of 2.005).[7,39] As a comparison, no obvious vacancy signals are observed in unmodified ZIS and ZIS/N-npG 1.0. With the formation of this 3D hierarchical nanoporous heterostructure, the strengthened sharper EPR signal of V_S-ZIS/N-npG could be ascribed to more exposed sulfur vacancies as electron capture centers.[38] Nonradiative S vacancies as active sites not only are conducive to the adsorption of H* but also are able to take part in the capturing of photoelectrons, so as to improve the intrinsic photocatalytic activity.[8,10,12] S vacancies provide channels for the injection of photoinduced electrons, thus avoiding the disadvantageous recombination of carriers. The specific surface area and pore size distribution diagrams of N-npG, V_S-ZIS and V_S-ZIS/N-npG 1.0 were explored by N_2 adsorption−desorption isotherms and BJH methods (Figure S6). The specific surface area of N-npG is calculated to be 363.18 $m^2\ g^{-1}$, and the average pore size is about 201.9 nm, indicating the characteristics of nanoporosity. Both V_S-ZIS and V_S-ZIS/N-npG 1.0 present a type IV isotherm with H2 hysteresis loops, and the specific surface area of V_S-ZIS/N-npG 1.0 (103.34 m^2/g) is much larger than pristine V_S-ZIS (40.81 m^2/g). The pore size distribution results in Figure S6d demonstrate that the mesopore character of V_S-ZIS/N-npG 1.0 becomes larger upon coupling V_S-ZIS with N-npG, which can be attributed to the dispersion of ZIS nanosheets on the surface and bicontinuous pore channel of N-npG. This result manifests that the as-designed 3D V_S-ZIS/N-npG heterojunction can effectively expose more active sites for the

https://doi.org/10.1021/jacsau.3c00482
JACS Au 2023, 3, 3127−3140

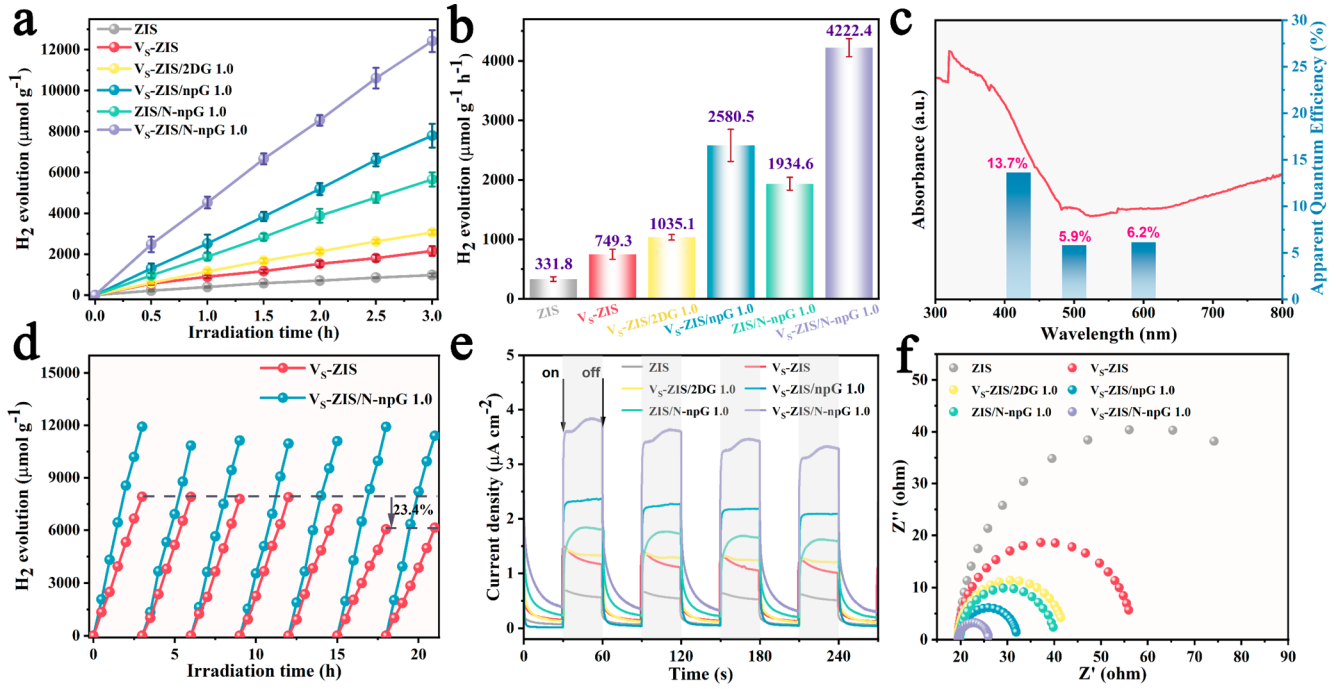

Figure 3. (a) Time-dependent profiles of photocatalytic H_2 evolution and (b) H_2 evolution rates of the as-prepared samples with three repeat experiments. (c) Wavelength-dependent apparent quantum efficiency (AQE) of V_S-ZIS/N-npG 1.0. (d) Recycling photocatalysis test of V_S-ZIS and V_S-ZIS/N-npG 1.0 with prolonged visible-light irradiation for seven cycles. (e) Transient photocurrent response plots and (f) Nyquist plots of EIS of ZIS, V_S-ZIS and composite material.

molecular adsorption and photocatalytic reaction, which is in accordance with EPR observations. Large surface area and curvature of 3D N-npG enables V_S-ZIS pieces to afford abundant exposure of accessible S vacancies as reactive sites.

Photocatalytic Performance Measurements

The performance of photocatalytic hydrogen production was evaluated in the system without an extra auxiliary catalyst under visible light illumination. The optimal stoichiometric ratio of Zn/In/S by varying the additive amount of TAA (Figure S7) as well as the weight percentage of N-npG (Figure S8) is obtained by the maximum hydrogen evolution rate owing to the abundant favorable exposure of active sites and efficient separation of carriers. As illustrated in Figure 3a and b, the introduction of S vacancies in the V_S-ZIS sample significantly improves the photocatalytic activity compared with ZIS. However, the V_S-ZIS/2DG 1.0 sample exhibits only inferior activity. Such findings manifest that loading V_S-ZIS nanosheets on the N-npG-forming 3D hierarchical heterostructures will lead to a notable advantageous influence on photocatalytic activity. In addition, the V_S-ZIS/npG 1.0 sample just possesses a modest improvement; thus, the modified electronic structure of graphene originating from the doping of nitrogen plays a role in the outstanding performance of V_S-ZIS/N-npG 1.0. Meanwhile, the HER performance of the ZIS/N-npG 1.0 sample without S vacancies as active sites is also just unsatisfactory. The V_S-ZIS/N-npG 1.0 photocatalyst exhibits a remarkable highest H_2-evolution rate of 12667.2 μmol after 3 h of photocatalytic reaction, which could be comparable with previously reported ZIS/graphene photocatalysts, as displayed in Table S1. Therefore, the superior catalytic activity of V_S-ZIS/N-npG 1.0 is derived from the synergistic effect of the as-designed 3D hierarchical heterojunction, sufficient S vacancies exposure and introduction of nitrogen species in undoped npG. The wavelength-dependent hydrogen evolution efficiency of V_S-ZIS/N-npG 1.0 was also tested for more valid comparison. As observed in Figure 3c, the AQE values of V_S-ZIS/N-npG 1.0 under different monochromatic light wavelengths are calculated to be 13.7% (420 nm), 5.9% (500 nm), and 6.2% (600 nm), respectively. The action spectrum of V_S-ZIS/N-npG 1.0 coincides well with the UV−vis spectrum, manifesting the favorable optical absorption and utilization capacity of the V_S-ZIS/N-npG 1.0 photocatalyst.

Moreover, cyclic stability is also an important factor that should be taken into consideration for practical application. After continuous operation for up to 20 h, V_S-ZIS/N-npG 1.0 retains superior stability as the photocatalytic hydrogen evolution rate exhibits no apparent decay, while bare V_S-ZIS shows about 23.4% attenuation (Figure 3d). It could be deduced that N-doped graphene as the substrate can enhance the photostability of V_S-ZIS and effectively improve photocorrosion of S^{2-} by photoinduced holes. The overall topological morphology and porous structure of V_S-ZIS/N-npG is well-kept, as illustrated in Figure S9a. Additionally, the XRD pattern of V_S-ZIS/N-npG 1.0 presents slight diffraction peak broadening, which could be attributed to the destruction of the edge of the nanosheet by photocorrosion for the decreased sample size, after repeated photocatalytic cycles in comparison with the fresh sample (Figure S9b). However, the crystal phase of the sample does not change obviously, which proves the decent structural stability of V_S-ZIS/N-npG 1.0. In this regard, high-resolution XPS measurements for V_S-ZIS and V_S-ZIS/N-npG 1.0 were further probed to investigate the chemical composition changes after durable photocatalysis for a more accurate analysis. In Figure S10, S 2p core levels of bare V_S-ZIS present an obvious shift (0.5 eV) to higher binding energy, which originates from S^{2-} self-oxidation to S^0 with a higher valence state by photoinduced holes. By contrast, V_S-

https://doi.org/10.1021/jacsau.3c00482
JACS Au 2023, 3, 3127−3140

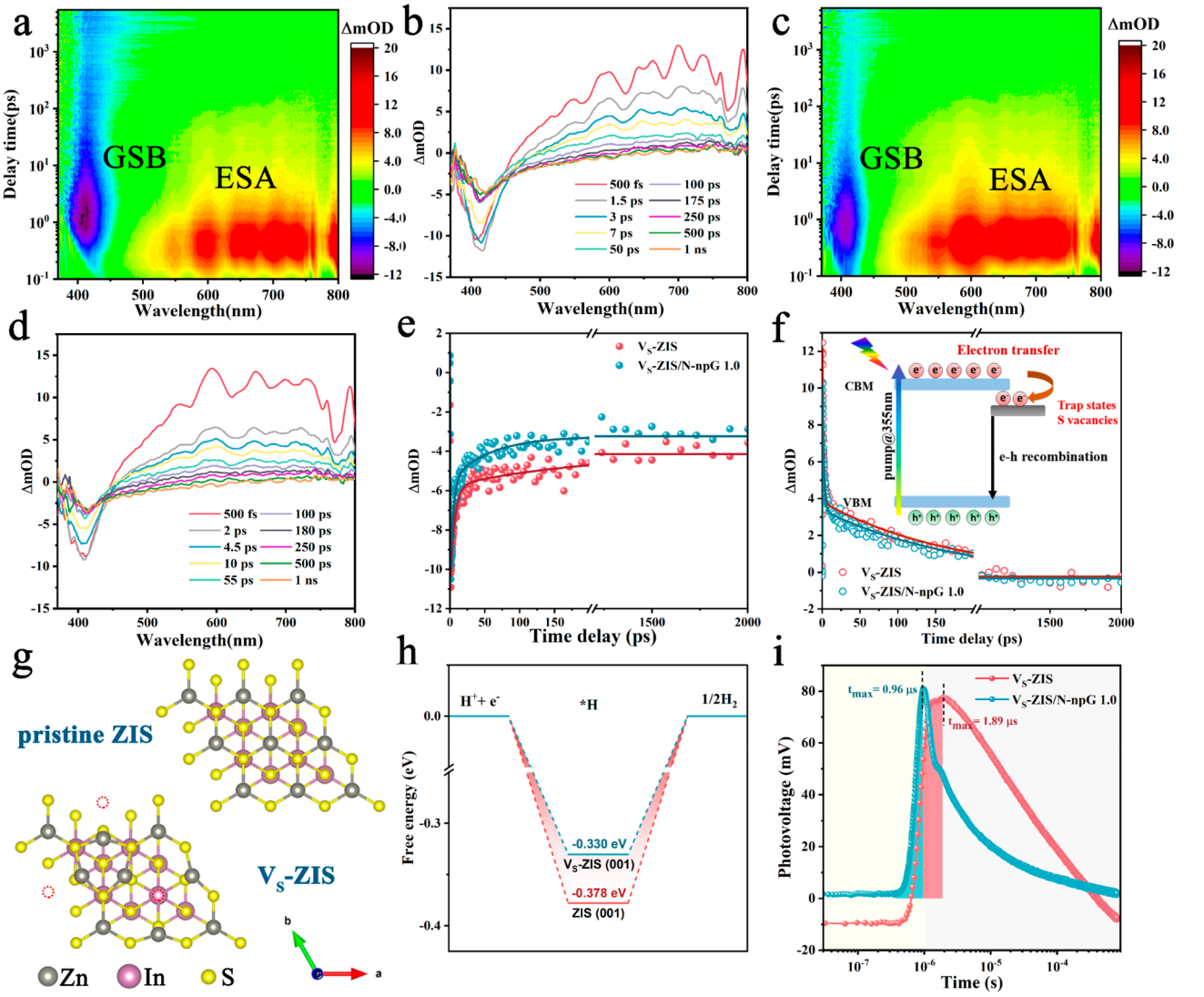

Figure 4. Femtosecond transient absorption (fs-TA) spectroscopy observation of 3D pseudo color spectra and corresponding 2D ultrafast spectral signal of (a, b) V_S-ZIS and (c, d) V_S-ZIS/N-npG 1.0. (e) Comparative kinetics decay curves monitoring at 409 nm in the GSB region. (f) Corresponding comparative kinetics decay curves monitoring at 650 nm in the ESA region. Inset: a concise diagrammatic drawing depicting the probable charge transfer mechanism occurring in V_S-ZIS with S vacancies. (g) Theoretical atomic configuration of pristine $ZnIn_2S_4$ (ZIS) and S-vacancy-rich $ZnIn_2S_4$ (V_S-ZIS) from top view after geometry optimization. (h) Gibbs free energy profiles for H atoms adsorption on ZIS and V_S-ZIS. (i) Transient-state surface photovoltage (TS-SPV) measurements of V_S-ZIS and V_S-ZIS/N-npG 1.0.

ZIS/N-npG 1.0 shows a negligible red-shift of the S^{2-}, demonstrating the suppressed photocorrosion reaction during long-time operation as well as well-maintained chemical composition. As a consequence, this well-designed 3D V_S-ZIS/N-npG heterojunction achieves high-activity and high-stability photocatalysis, and N-npG as the supporting matrix leads to effectively inhibited photocorrosion of $ZnIn_2S_4$ under long visible-light irradiation.

Measurement of Charge Separation and Proposed Photocatalytic Mechanism

To better understand the underlying mechanism of the enhanced photocatalytic performance, related optical characterizations were performed. As depicted in Figure S11a, marked enhancement in the light harvesting capability is observed after 480 nm after the introduction of N-npG as a supporting matrix. Meanwhile, there is no absorption edge in the spectrum of N-npG, which is a typical characteristic of the zero-bandgap semimetallic material. N-npG does not possess the photocatalytic hydrogen evolution capability, so the enhanced light absorption and utilization capacity could be indexed to the three-dimensional bicontinuous nanoporous structure of N-npG via multiple reflection and scattering.[40] According to the Kubelka–Munk formula, $(\alpha h\nu)^2 = K(h\nu - E_g)$, α represents the absorption coefficient, h is the Planck constant, ν is the photon's frequency, and $h\nu$ means the incident photon energy; for a direct bandgap semiconductor material,[41] the band gap (E_g) of V_S-ZIS is measured to be 2.44 eV (Figure S11b).

The behavior of photogenerated electron–hole pairs was investigated by steady-state PL spectra. The obvious PL quenching of V_S-ZIS/N-npG 1.0 in comparison with ZIS and V_S-ZIS is uncovered in Figure S12a. The PL intensity of V_S-ZIS is weaker than that of pristine ZIS, presumably due to the capture of electrons through S vacancies inhibiting the recombination of electrons and holes. Meanwhile, the dramatically decreased PL emission peak intensity of V_S-ZIS/

https://doi.org/10.1021/jacsau.3c00482
JACS Au 2023, 3, 3127–3140

N-npG 1.0 indicates the suppressed excited state decay in this 3D heterostructure photocatalyst, indicating the sufficient existence of reactive species.[42] Furthermore, TRPL decay profiles were applied to elucidate the charge separation photodynamics in Figure S12b. The decay process was fitted by the biexponential decay kinetics equation, the faster lifetime factor τ_1 is caused by the interband nonradiative recombination of free excitons and charge transfer processes, while the long lifetime factor τ_2 reflects the radiative recombination process of carriers.[43,44] As displayed in detail in the inset of Figure S12b, for the single ZIS and V_S-ZIS, the slow decay component τ_2 related to radiative recombination is significantly prolonged (5.34 ns for ZIS vs 10.41 ns for V_S-ZIS), meaning an elongated lifetime of active charge carriers in V_S-ZIS after the introduction of S vacancies. Moreover, the distinctly accelerated τ_1 fast decay parameter related to charge transfer and increased proportion indicate enhanced separation and transfer efficiency of photogenerated carriers in the V_S-ZIS/N-npG (τ_1 = 0.84 ns, τ_2 = 5.52 ns) heterojunction in comparison with the bare V_S-ZIS (τ_1 = 1.10 ns, τ_2 = 10.41 ns). V_S-ZIS/N-npG 1.0 processes a shorter average lifetime (τ_A) of 2.66 ns, compared to 5.90 ns for bare V_S-ZIS, manifesting that photogenerated carriers can be separated and migrated efficiently in the heterojunction. The existence of an efficient carrier migration process is related to fluorescence quenching behavior, which will shorten the fluorescence lifetime.[45,46] The apparent PL quenching and corresponding accelerated decay demonstrate that rapid migration and separation of charge carriers are achieved in the V_S-ZIS/N-npG heterojunction. To further verify the enhanced interfacial charge transfer behaviors, transient photocurrent response curves (I−t) and electrochemical impedance spectroscopy (EIS) were studied, as illustrated in Figure 3e−f and Figure S13. The photocurrent intensity observed under visible-light illumination matches the hydrogen generation efficiency (Figure 3e). In comparison with V_S-ZIS/npG 1.0, ZIS/N-npG 1.0 and V_S-ZIS/2DG 1.0, the strongest photocurrent density of V_S-ZIS/N-npG 1.0 implies the most efficient charge separation capability in the heterostructure. Therefore, it could be concluded that not only more exposed S vacancies as active sites originating from the 3D bicontinuous porous supporting matrix but also the N-doped graphene are in favor of the interfacial carrier separation. Correspondingly, this result can be further confirmed by EIS spectra; the V_S-ZIS/N-npG 1.0 presents the smallest high-frequency semicircle in the Nyquist plots (Figure 3f and Figure S13b), suggesting its reduced charge-transport resistance for efficient utilization of photogenerated electrons. These photoelectrochemical tests reveal that the formation of the 3D hierarchical nanoporous heterostructure and intimate interface interaction are conducive to promoting the transportation of charge carriers in V_S-ZIS/N-npG, thus ensuring the high-efficiency separation of photogenerated electron−hole pairs.

In addition, as an in-depth step to elucidate the dynamic behaviors of photogenerated electrons and holes, the femtosecond transient absorption (fs-TA) spectroscopy and transient-state SPV (TS-SPV) were performed on individual V_S-ZIS as well as V_S-ZIS/N-npG hierarchical heterosystems. The 3D contour plots and corresponding 2D ultrafast spectral signals for fs-TA spectra of the Vs-ZIS and V_S-ZIS/N-npG heterojunction are displayed in Figure 4a−d. Excitons in V_S-ZIS are excited by using a 355 nm pumped laser. Both the pristine V_S-ZIS and V_S-ZIS/N-npG heterojunctions display similar negative ground state bleaching (GSB) signals at a range of 370−460 nm and positive transient excited state absorption (ESA) signals with a scope of 500−800 nm. As the photogenerated carriers are pumped to an excited state with high-energy pump photons (355 nm, 3.49 eV), resulting in the decrease of the ground state distribution, a negative signal is generated in the wavelength region. The GSB feature peaks with maximum bleach wavelengths located around 409 nm could be ascribed to the bleaching of a higher order singlet exciton for both V_S-ZIS and V_S-ZIS/N-npG.[47] For the 2D ultrafast spectral signal of V_S-ZIS/N-npG, the bleaching signals become weaker while the absorption signals appear to be stronger, which suggests the possible flow out and neutralization of photoinduced holes in the valence band of V_S-ZIS to N-npG (Figure 4b and d).[48]

The detailed dynamic behaviors of photogenerated carriers probed at the GSB region are basically different as displayed in Figure 4e. The attenuation curves of kinetics are characterized via biexponential fitting in which τ_{GSB1} and τ_{GSB2} could be indexed to the trap-assisted nonradiative recombination and the interband electron−hole radiative recombination.[49−51] Relative parameters are listed in Table S2: τ_{GSB1} = 7.19 ps (80.4%) and τ_{GSB2} = 253 ps (19.6%) for V_S-ZIS, while V_S-ZIS/N-npG presents a shorter lifetime (τ_{GSB1} = 4.38 ps (69%) and τ_{GSB2} = 58 ps (31%)), which is consistent with the TRPL results. The components of both radiative and nonradiative recombination processes are accelerated, and the dramatically expedited τ_{GSB2} components indicate efficient carrier migration and separation behavior in the V_S-ZIS/N-npG heterojunction. The average recovery time τ_{GSB-A} is estimated to be 50.28 ps for the V_S-ZIS/N-npG heterojunction system (vs 227.34 ps for V_S-ZIS). Such a significant lifetime decrease originating from the rapid exciton relaxation mechanism could be mainly attributed to the additional emerged channel for the interfacial charge transfer for hole extraction to promote the separation efficiency.[45,48,52]

Widened positive excited state absorption (ESA) features indicate the presence of long excited states. According to previous reports in the literature, this positive characteristic signal can be attributed to the photoinduced absorption of photogenerated electrons trapped in the shallow defect states.[8,39,53] To determine the exciton relaxation process of the ESA state, the corresponding kinetics is monitored subsequently by probing at 650 nm as representative data, as shown in Figure 4f. In terms of the bandgap trap state schematic diagram in the inset of Figure 4f, the procedures of relaxation could be understandable. Under the circumstances, the faster decay factor τ_{ESA1} (∼1.49 ps) manifests the shallow capture of the electrons by the interband sulfur vacancies defect in V_S-ZIS, while the recombination process of photogenerated carriers is reflected by the much more sluggish decay factor τ_{ESA2} (∼174 ps).[54−58] The lifetime component τ_{ESA2} for recombination of electrons at shallow trap sites is slightly prolonged for an efficacious photocatalytic process (∼1.84 ps (67%), ∼179 ps (33%)), as demonstrated in detail in Table S3. Note that there is no significant difference in decay lifetime components (τ_{ESA1}, τ_{ESA2}) and average recovery lifetime between V_S-ZIS (τ_{ESA-A} = 170.54 ps) and V_S-ZIS/N-npG (τ_{ESA-A} = 175.34 ps) in the ESA region. It can be inferred that sulfur vacancies always act as defect states to promote electron−hole separation in both the individual V_S-ZIS and the as-formed heterojunction, which further proves that sulfur vacancies serve as the active sites, as discussed above. The

https://doi.org/10.1021/jacsau.3c00482
JACS Au 2023, 3, 3127−3140

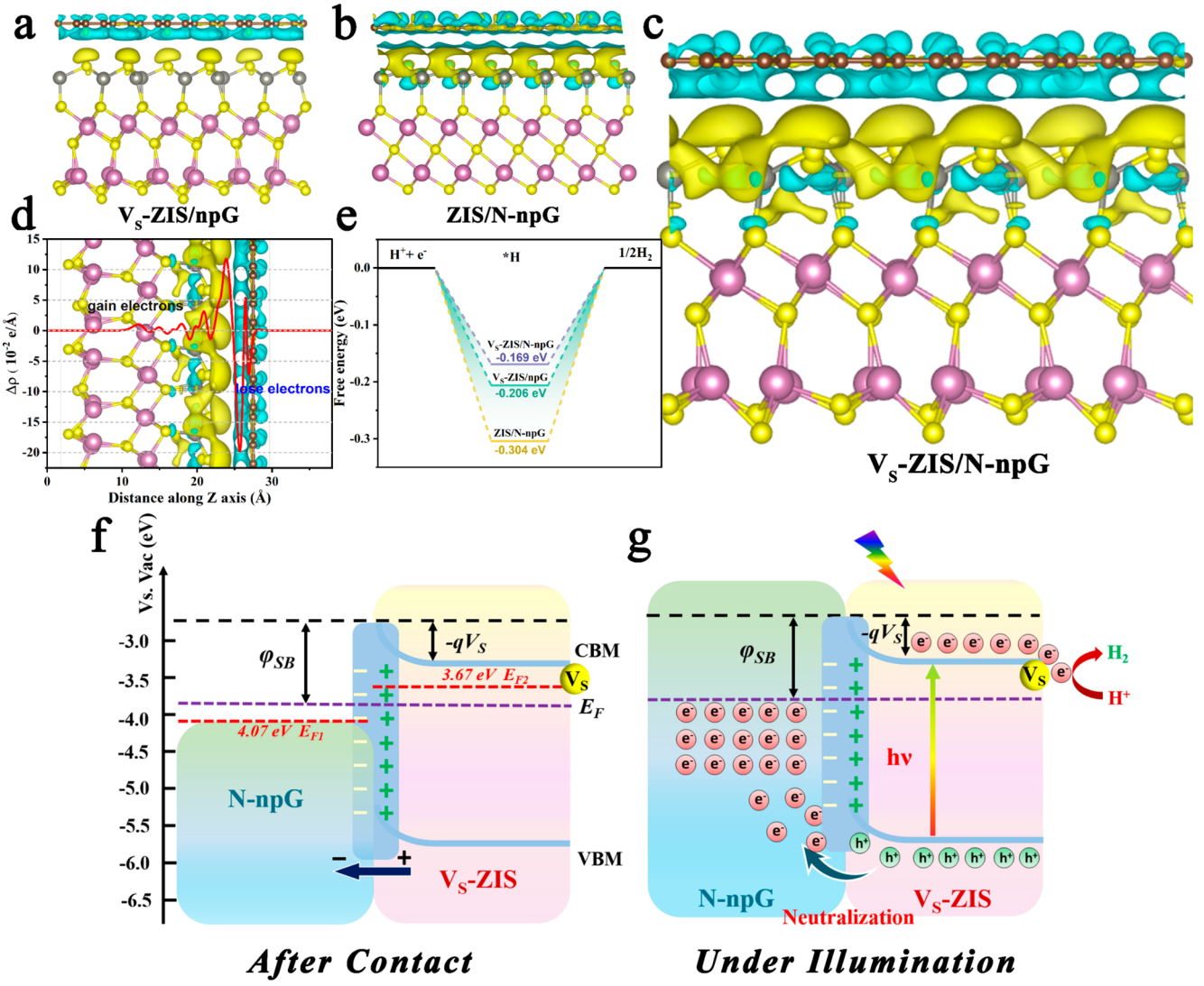

Figure 5. 3D differential charge density distribution diagrams of (a) V_S-ZIS/npG, (b) ZIS/N-npG, and (c) V_S-ZIS/N-npG, where yellow and cyan regions represent accumulation and depletion of electrons, respectively. (d) Corresponding plane-averaged differential charge density distribution map along the *Z* direction for the V_S-ZIS/N-npG heterojunction. (e) Calculated H atom adsorption Gibbs free energy profiles of V_S-ZIS/npG, ZIS/N-npG and V_S-ZIS/N-npG. Energy level alignment schemes illustrating the charge transfer in V_S-ZIS/N-npG heterojunction (f) after contact and (g) under illumination for photocatalytic water spitting process (φ_{SB} represents the barrier at the N-npG side, while $-qV_S$ means the barrier at the V_S-ZIS side).

working mechanism of sulfur (S) vacancies in V_S-ZIS gains further insight from theoretical calculations of density functional theory (DFT). Theoretical atomic configurations after geometry optimization of pristine $ZnIn_2S_4$ (ZIS) and S-vacancy-rich $ZnIn_2S_4$ (V_S-ZIS) from the top view are presented in Figure 4g. In general, an adsorption free energy closer to zero representing the subtle balance between hydrogen adsorption and desorption has been universally accepted as a descriptor for superior catalytic hydrogen evolution activity.[59,60] The Gibbs free energies of ZIS and V_S-ZIS were compared and are summarized in Figure 4h and Table S4, manifesting that the intrinsic catalytic active sites for hydrogen evolution are predominately contributed by S vacancies. The absolute value of adsorption free energy of H atoms (ΔG_{H^*}) at the S vacancies sites in V_S-ZIS (−0.330 eV) is smaller than that of the pristine ZIS (−0.378 eV). Both the experimental and theoretical calculation results illustrate the positive effect of S vacancies which efficiently provide a shallow defect energy level for trapping electrons and accelerate the catalytic reaction kinetics of hydrogen generation.

TS-SPV measurements from the nanosecond to millisecond were also probed upon the excitation of a 355 nm laser to clarify the defect-related charge-separation processes and differentiate them from charge separation arising from a surface built-in electric field or other means, as displayed in Figure 4i. A negative TS-SPV signal is monitored in V_S-ZIS at the initial scale shorter than the nanosecond scale, which means more photogenerated electrons migrate to the surface of V_S-ZIS. At longer times, the surface voltage changes from negative to positive for V_S-ZIS with the prolonging of time at higher photon energies. The reversed SPV signals rationalized SPV variations for V_S-ZIS were probably associated with S vacancy induced electron trapping, while more photogenerated holes are transferred from the bulk to the surface.[61] Defect-induced charge separation occurs at longer times, thereby leading to an inversion of charge separation at the microsecond time scale. Meanwhile, S vacancy mediated charge separation

https://doi.org/10.1021/jacsau.3c00482
JACS Au 2023, 3, 3127−3140

occurs in both V_S-ZIS and V_S-ZIS/N-npG. As for the signal at a time longer than 10^{-6} s corresponding to the typical time scale of the diffusion photovoltage, the absolute value of the TS-SPV signal of V_S-ZIS/N-npG is reduced in comparison with the pristine specimen. This result could be attributed to the hole neutralization behaviors with respect to the recombination of photoholes generated in V_S-ZIS with extra free electrons in N-npG. Additionally, a smaller t_{max} and integral area of the shadow part representing a fast charge extraction process is observed in V_S-ZIS/N-npG, which also proves the presence of an efficient charge extraction path.[6,62] S vacancies initiate charge separation by generating shallow defect energy levels and stabilize the charge separation state by trapping the photogenerated electrons. In contrast, the introduction of electron-rich N-npG, as an electron donor, results in hole neutralization behaviors that directly induce a charge-separation process on the surface. It provides a shred of forward evidence for the construction of a specific transfer path in which photogenerated holes are extracted from V_S-ZIS to N-npG at the heterojunction interface region.[63,64]

The rearrangement behaviors of charge carriers at the heterointerfaces for V_S-ZIS/npG, ZIS/N-npG and V_S-ZIS/N-npG were investigated by observing the differential charge density distribution, as shown in Figure 5a−c. Theoretical computational models for the calculation are presented in Figure S14. Originating from the strong electron-withdrawing capacity of S vacancies, the electrons on $ZnIn_2S_4$ are more inclined to be trapped and localized at V_S-ZIS domains (Figure 5a). When ZIS is coupled with nitrogen-doped graphene in Figure 5b, the vicinity of S sites presents slightly decreased electron density. However, due to the n-type doping of an electron-rich nitrogen heteroatom to introduce extra electrons, ZIS still appears to have electron accumulation on a large scale at the interface region, while pronounced electron depletion is observed at the N-npG side. As for V_S-ZIS/N-npG (Figure 5c), the planar-averaged charge density difference along the Z axis is given in Figure 5d to intuitively display the variation of the charge density. The designed interfacial charge rearrangement including increased local electron density at V_S-ZIS and electron depletion at N-npG corroborates the intense interaction and the regulation of interfacial electronic structure.[65] Notably, the increased accumulated electrons observed on the S vacancy position provides further evidence for the sulfur vacancies serving as electrons traps. For photocatalysis, S vacancies as a shallow defect energy level are capable of capturing electrons, while electron-rich N-npG benefits the electrons donation and possesses the tendency of photogenerated holes extraction and neutralization from V_S-ZIS to N-npG.

Hydrogen adsorption Gibbs free energy (ΔG_{H^*}) was further explored to verify the H adsorption and desorption behaviors at the catalytic sites. Tracing to Figure 4h, the obtained ΔG_{H^*} value of ZIS shows the strong interaction between H* and ZIS, which is not conducive to the H_2 generation, leading to a relatively large ΔG_{H^*} absolute value of −0.378 eV. The corresponding ΔG_{H^*} values of V_S-ZIS/npG, ZIS/N-npG and V_S-ZIS/N-npG are −0.206, −0.304, and −0.169 eV, respectively (Figure 5e). The introduction of sulfur vacancies as catalytically active sites greatly improves the hydrogen desorption kinetics in composite samples. The theoretical calculation results are in good accordance with the experimental data for practical hydrogen evolution. The V_S-ZIS/N-npG (−0.169 eV) is corroborated to be more practicable to achieve the equilibrium of hydrogen adsorption and desorption. S vacancies in V_S-ZIS and the introduced N dopants in graphene are favorable for hydrogen desorption.

In light of the above results and analyses, the band structure alignment over the V_S-ZIS/N-npG heterojunction is discussed below, aiming to clarify the enhanced photogenerated carriers' separation process and underlying photocatalytic mechanism. The concrete energy band structure of V_S-ZIS was ascertained by UPS spectra (Figure S15) and UV−vis DRS techniques. As calculated from the difference between the secondary cutoff energy (E_{cutoff}) and the photon energy of the exciting radiation,[66] the work function (Φ) value of V_S-ZIS measured based on UPS is determined to be 3.67 eV, which is smaller than previous reports. The introduction of S vacancies or other nonmetallic impurities may move the position of Fermi energy toward the conduction band direction, thereby reducing the work function of the semiconductor.[67] It could be deduced that there is a higher potential barrier between V_S-ZIS with abundant S vacancies and N-npG after contact. According to the formula $E_{VB} = E_{edge} + \Phi$, the valence band position of V_S-ZIS is determined to be −5.75 eV vs V_{ac}. Moreover, based on the bandgap value (E_g) of V_S-ZIS (2.44 eV), the conduction band edge is estimated to be −3.31 eV vs V_{ac}. After contact for equilibrium, the work function (Φ) value is determined to be 3.88 eV for V_S-ZIS/N-npG, and the position of the Fermi level is situated between the two (Figure S15b). The UPS test demonstrates that the energy level accords with the characteristics of Schottky junction with favorable energy band alignment. Besides, Mott−Schottky measurements for the observation of the carrier concentration's change support the formation of the V_S-ZIS/N-npG heterojunction. As displayed in Figure S15c, the flat band potential of V_S-ZIS is about −0.89 V vs RHE, which coincides with the UPS and UV−vis tests for the determination of energy level position.[68] The slope of the linear region for V_S-ZIS/N-npG is smaller than V_S-ZIS, meaning high carrier concentration and electron mobility, which provides evidence for the successful formation of the heterojunction.[69,70]

The adaptive energy level structure after contact is schematically illustrated in Figure 5f. The Schottky junction with the space charge region is formed after contact because electrons flow from V_S-ZIS to semimetallic N-npG. The formation of the internal electric field causes the energy of electrons on the surface of V_S-ZIS to be higher than in the body; thus, the energy band is bent upward. Along with achieving equilibrium, the Fermi levels of N-npG and V_S-ZIS are at the same level, and there is no more net flow of electrons. The energy band edge of V_S-ZIS bends upward to form a Schottky barrier with a height of φ_{SB}. When V_S-ZIS is subjected to visible sunlight irradiation (Figure 5g), the electrons generated in the valence band (VB) could be motivated to the conduction band (CB), and photogenerated hole species have remained in the VB. Due to the existence of a discrete defect energy-level (DEL) interband of V_S-ZIS and potential barrier at the heterojunction interface, the photogenerated electrons are more inclined to be captured by S vacancies shallow trap state. Benefiting from the suitable thermodynamic potential for photocatalytic hydrogen evolution, the trapped electrons could migrate toward the surface to participate in the specific photocatalytic reaction with H^+ kinetically. Besides, the nitrogen dopant endows graphene with a relatively strong electron-donating ability and delivers an electron-rich state. The extra free electrons in N-npG may

https://doi.org/10.1021/jacsau.3c00482
JACS Au 2023, 3, 3127−3140

neutralize the holes in the valence band of V_S-ZIS, while photogenerated electrons are still localized at V_S-ZIS domains. During photocatalysis, the formed built-in electric field with an upward band bending barrier could block the jump of photogenerated electrons while allowing the photogenerated holes to be collected by N-npG. Meanwhile, photogenerated electrons are potentially captured by the S vacancy and localized at the V_S-ZIS domain to allow the reduction reaction to occur on account of the strong electron-withdrawing ability of S vacancies in V_S-ZIS. Consequently, hydrogen intermediates are preferentially adsorbed on the sulfur vacancy of V_S-ZIS, abundant photogenerated electrons, strong reduction capacity and high intrinsic activity could efficiently activate water molecules to generate H_2, while the sufficient photogenerated holes remaining in the VB of V_S-ZIS are depleted by the Na_2S/Na_2SO_3 sacrificial agent. The intimate contact between V_S-ZIS and N-npG leads to a more efficient interface charge transfer. As such, extremely high-efficiency photogenerated carrier separation brings up decent photocatalytic hydrogen evolution activity and excellent photocatalytic stability.

CONCLUSIONS

To summarize, a 3D hierarchical heterostructure is constructed consisting of S-vacancy-rich ZIS (V_S-ZIS) and N-doped nanoporous graphene associated with tailored photodynamic behaviors. The deep principle of sulfur vacancies as active sites for enhanced carrier separation is revealed with in situ dynamic study. Under the formed built-in electric field with an upward band bending barrier, photogenerated electrons are captured by the S vacancies in V_S-ZIS effectively to participate in the hydrogen generation reaction, while the interfacial holes are neutralized by the extra free electron in N-npG to restrain self-corrosion. Efficient visible-light utilization and sufficient active site exposure are guaranteed by a well-fitted nanoporous heterostructure. Theoretical calculations provide evidence for the available manipulation of the interfacial charge distribution and optimized desorption kinetic energies of H* for hydrogen generation. The unique 3D hierarchical heterostructure with the high separation efficiency of photogenerated electrons and holes endows this system with superior photocatalytic performance, inspiring the designs of capture and trapping photocatalytic systems in other research fields.

ASSOCIATED CONTENT

Supporting Information

The Supporting Information is available free of charge at https://pubs.acs.org/doi/10.1021/jacsau.3c00482.

Experimental details including in situ XPS test, apparent quantum efficiency measurements, fs-TA spectroscopy measurement, photoelectrochemical measurements, and computational methods; SEM and TEM images, XRD patterns, Raman spectra, XPS/UPS survey spectra, BET isotherms, UV−vis DRS results, and M-S test results; H_2 evolution rate of $ZnIn_2S_4$ synthesized by adding different amounts of TAA and H_2 evolution rates and I−t/EIS plots of V_S-ZIS/N-npG with various N-npG masses; and PL and TRPL decay spectra and kinetic fitting results of fs-TA spectra (PDF)

AUTHOR INFORMATION

Corresponding Author

Yongzheng Zhang − *School of Physics and Physical Engineering, Qufu Normal University, Qufu 273165, China;* orcid.org/0000-0003-3322-8952; Email: yzzhang@qfnu.edu.cn

Authors

Chunyu Yuan − *School of Physics and Physical Engineering, Qufu Normal University, Qufu 273165, China*

Hongfei Yin − *School of Physics and Physical Engineering, Qufu Normal University, Qufu 273165, China*

Huijun Lv − *School of Physics and Physical Engineering, Qufu Normal University, Qufu 273165, China*

Yujin Zhang − *School of Physics and Physical Engineering, Qufu Normal University, Qufu 273165, China*

Jing Li − *Key Laboratory of Photochemical Conversion and Optoelectronic Materials, Technical Institute of Physics and Chemistry, Chinese Academy of Sciences, Beijing 100190, China;* orcid.org/0000-0002-0227-0392

Dongdong Xiao − *Institute of Physics, Chinese Academy of Sciences, Beijing 100190, China*

Xiaoyong Yang − *School of Physics and Physical Engineering, Qufu Normal University, Qufu 273165, China; Condensed Matter Theory Group, Materials Theory Division, Department of Physics and Astronomy, Uppsala University, 75120 Uppsala, Sweden;* orcid.org/0000-0001-5024-1361

Ping Zhang − *School of Physics and Physical Engineering, Qufu Normal University, Qufu 273165, China*

Complete contact information is available at: https://pubs.acs.org/10.1021/jacsau.3c00482

Author Contributions

Chunyu Yuan conceptualization, data curation, formal analysis, investigation, methodology, resources, software, validation, visualization, writing-original draft; **Hongfei Yin** data curation, formal analysis, investigation, software, validation, visualization; **Huijun Lv** data curation, formal analysis, investigation, validation; **Yujin Zhang** data curation, formal analysis, investigation, validation; **Jing Li** data curation, investigation, software, validation, visualization; **Dongdong Xiao** data curation, investigation, resources, validation; **Xiaoyong Yang** data curation, formal analysis, funding acquisition, investigation, software, validation; **Yongzheng Zhang** conceptualization, data curation, formal analysis, funding acquisition, investigation, methodology, project administration, resources, supervision, validation, visualization, writing-review & editing; **Ping Zhang** conceptualization, data curation, formal analysis, funding acquisition, investigation, project administration, resources, validation, writing-review & editing.

Funding

This work was supported by the Higher Educational Youth Innovation Science and Technology Program Shandong Province (2021KJ022), Taishan Scholars Program (tsqn201909107), Shandong Province Natural Science Foundation (ZR2020QF077) and National Natural Science Foundation of China (62104131), National Natural Science Foundation of China, Grant No. 11705152, Shandong Provincial Excellent Youth Science Fund Project. The National

Key R&D Program of China (Grant No. 2021YFB3802900). The Major Program of National Natural Science Foundation of China (Grant No. 52192604).

Notes

The authors declare no competing financial interest.

REFERENCES

(1) Fujishima, A.; Rao, T. N.; Tryk, D. A. Titanium dioxide photocatalysis. *J. Photoch. Photobio. C* **2000**, *1*, 1−21.
(2) Takata, T.; Jiang, J.; Sakata, Y.; Nakabayashi, M.; Shibata, N.; Nandal, V.; Seki, K.; Hisatomi, T.; Domen, K. Photocatalytic water splitting with a quantum efficiency of almost unity. *Nature.* **2020**, *581*, 411−414.
(3) Yao, Q.; Li, H.; Xue, J.; Jiang, S.; Zhang, Q.; Bao, J. Promoting photocatalytic H_2 evolution through retarded charge trapping and recombination by continuously distributed defects in methylammonium lead Iodide perovskite. *Angew. Chem., Int. Ed.* **2023**, *62*, No. e202308140.
(4) Yang, R.; Mei, L.; Fan, Y.; Zhang, Q.; Zhu, R.; Amal, R.; Yin, Z.; Zeng, Z. $ZnIn_2S_4$-based photocatalysts for energy and environmental applications. *Small Methods* **2021**, *5*, 2100887.
(5) Xu, L.; Deng, X.; Li, Z. Photocatalytic splitting of thiols to produce disulfides and hydrogen over $PtS/ZnIn_2S_4$ nanocomposites under visible light. *Appl. Catal., B* **2018**, *234*, 50−55.
(6) Yu, K.; Zhang, T.; Wang, Y.; Wu, J.; Huang, H.; Yin, K.; Liao, F.; Liu, Y.; Kang, Z. Anchoring Co_3O_4 on CdZnS to accelerate hole migration for highly stable photocatalytic overall water splitting. *Appl. Catal. B: Environ.* **2023**, *324*, 122228.
(7) Du, C.; Zhang, Q.; Lin, Z.; Yan, B.; Xia, C.; Yang, G. Half-unit-cell $ZnIn_2S_4$ monolayer with sulfur vacancies for photocatalytic hydrogen evolution. *Appl. Catal., B* **2019**, *248*, 193−201.
(8) Jing, X.; Lu, N.; Huang, J.; Zhang, P.; Zhang, Z. One-step hydrothermal synthesis of S-defect-controlled $ZnIn_2S_4$ microflowers with improved kinetics process of charge-carriers for photocatalytic H_2 evolution. *J. Energy Chem.* **2021**, *58*, 397−407.
(9) Wang, X.; Wang, X.; Huang, J.; Li, S.; Meng, A.; Li, Z. Interfacial chemical bond and internal electric field modulated Z-scheme Sv-$ZnIn_2S_4/MoSe_2$ photocatalyst for efficient hydrogen evolution. *Nat. Commun.* **2021**, *12*, 4112.
(10) Qin, Y.; Li, H.; Lu, J.; Feng, Y.; Meng, F.; Ma, C.; Yan, Y.; Meng, M. Synergy between van der waals heterojunction and vacancy in $ZnIn_2S_4/g\text{-}C_3N_4$ 2D/2D photocatalysts for enhanced photocatalytic hydrogen evolution. *Appl. Catal., B* **2020**, *277*, 119254.
(11) Jiang, R.; Cai, X.; Gu, X.; Yang, D.; Zhang, J.; Zhao, Y.; Mao, L. Photocatalytic H_2 evolution over sulfur vacancy-rich $ZnIn_2S_4$ hierarchical microspheres under visible light. *J. Mater. Sci.* **2021**, *56*, 19439−19451.
(12) Zhang, G.; Yuan, X.; Xie, B.; Meng, Y.; Ni, Z.; Xia, S. S vacancies act as a bridge to promote electron injection from Z-scheme heterojunction to nitrogen molecule for photocatalytic ammonia synthesis. *Chem. Eng. J.* **2022**, *433*, 133670.
(13) Su, T.; Men, C.; Chen, L.; Chu, B.; Luo, X.; Ji, H.; Chen, J.; Qin, Z. Sulfur vacancy and Ti3C_2T_x cocatalyst synergistically boosting interfacial charge transfer in 2D/2D $Ti_3C_2T_x/ZnIn_2S_4$ heterostructure for enhanced photocatalytic hydrogen evolution. *Adv. Sci.* **2022**, *9*, 2103715.
(14) Ito, Y.; Qiu, H. J.; Fujita, T.; Tanabe, Y.; Tanigaki, K.; Chen, M. Bicontinuous nanoporous N-doped graphene for the oxygen reduction reaction. *Adv. Mater.* **2014**, *26*, 4145−4150.
(15) Ito, Y.; Tanabe, Y.; Qiu, H. J.; Sugawara, K.; Heguri, S.; Tu, N. H.; Huynh, K. K.; Fujita, T.; Takahashi, T.; Tanigaki, K.; Chen, M. High-quality three-dimensional nanoporous graphene. *Angew. Chem., Int. Ed.* **2014**, *53*, 4822−4826.
(16) Kuang, P.; Sayed, M.; Fan, J.; Cheng, B.; Yu, J. 3D graphene-based H_2 production photocatalyst and electrocatalyst. *Adv. Energy Mater.* **2020**, *10*, 1903802.
(17) Xia, Y.; Cheng, B.; Fan, J.; Yu, J.; Liu, G. Near-infrared absorbing 2D/3D $ZnIn_2S_4$/N-doped graphene photocatalyst for highly efficient CO_2 capture and photocatalytic reduction. *Sci. China Mater.* **2020**, *63*, 552−565.
(18) Bie, C.; Yu, H.; Cheng, B.; Ho, W.; Fan, J.; Yu, J. Design, fabrication, and mechanism of nitrogen-doped graphene-based photocatalyst. *Adv. Mater.* **2021**, *33*, 2003521.
(19) Chang, D. W.; Baek, J. B. Nitrogen-doped graphene for photocatalytic hydrogen generation. *Chem. Asian J.* **2016**, *11*, 1125−1137.
(20) Mou, Z.; Wu, Y.; Sun, J.; Yang, P.; Du, Y.; Lu, C. TiO_2 nanoparticles-functionalized N-doped graphene with superior interfacial contact and enhanced charge separation for photocatalytic hydrogen generation. *ACS Appl. Mater. Interfaces* **2014**, *6*, 13798−806.
(21) Wang, X.; Sun, G.; Routh, P.; Kim, D.-H.; Huang, W.; Chen, P. Heteroatom-doped graphene materials: syntheses, properties and applications. *Chem. Soc. Rev.* **2014**, *43*, 7067−7098.
(22) Panchakarla, L.; Subrahmanyam, K.; Saha, S.; Govindaraj, A.; Krishnamurthy, H.; Waghmare, U.; Rao, C. Synthesis, structure, and properties of boron-and nitrogen-doped graphene. *Adv. Mater.* **2009**, *21*, 4726−4730.
(23) Wang, J.; Sun, S.; Zhou, R.; Li, Y.; He, Z.; Ding, H.; Chen, D.; Ao, W. A review: synthesis, modification and photocatalytic applications of $ZnIn_2S_4$. *J. Mater. Sci. Technol.* **2021**, *78*, 1−19.
(24) Wu, L.; Li, M.; Zhou, B.; Xu, S.; Yuan, L.; Wei, J.; Wang, J.; Zou, S.; Xie, W.; Qiu, Y.; Rao, M.; Chen, G.; Ding, L.; Yan, K. Reversible stacking of 2D $ZnIn_2S_4$ atomic layers for enhanced photocatalytic hydrogen evolution. *Small* **2023**, *19*, 2303821.
(25) Yang, R.; Mei, L.; Fan, Y.; Zhang, Q.; Zhu, R.; Amal, R.; Yin, Z.; Zeng, Z. $ZnIn_2S_4$ based photocatalysts for energy and environmental applications. *Small Methods* **2021**, *5*, 2100887.
(26) Zhang, Y.; Du, J.; Wang, Z.; Luo, M.; Tian, Y.; Fujita, T.; Xue, Q.; Chen, M. Three-dimensional nanoporous heterojunction of monolayer MoS_2@rGO for photoenhanced hydrogen evolution reaction. *ACS Appl. Energy Mater.* **2018**, *1*, 2183−2191.
(27) Ye, L.; Fu, J.; Xu, Z.; Yuan, R.; Li, Z. Facile one-pot solvothermal method to synthesize sheet-on-sheet reduced graphene oxide (RGO)/$ZnIn_2S_4$ nanocomposites with superior photocatalytic performance. *ACS Appl. Mater. Interfaces* **2014**, *6*, 3483−3490.
(28) Bie, C.; Zhu, B.; Xu, F.; Zhang, L.; Yu, J. In situ grown monolayer N-doped graphene on CdS hollow spheres with seamless contact for photocatalytic CO_2 reduction. *Adv. Mater.* **2019**, *31*, 1902868.
(29) Han, Y.; Fan, X.; Wang, H.; Zhao, F.; Tully, C. G.; Kong, J.; Yao, N.; Yan, N. High-yield monolayer graphene grids for near-atomic resolution cryoelectron microscopy. *P. Natl. Acad. Sci. USA* **2020**, *117*, 1009−1014.
(30) Giangregorio, M. M.; Jiao, W.; Bianco, G. V.; Capezzuto, P.; Brown, A. S.; Bruno, G.; Losurdo, M. Insights into the effects of metal nanostructuring and oxidation on the work function and charge transfer of metal/graphene hybrids. *Nanoscale.* **2015**, *7*, 12868−12877.
(31) Al-Gaashani, R.; Najjar, A.; Zakaria, Y.; Mansour, S.; Atieh, M. A. XPS and structural studies of high quality graphene oxide and reduced graphene oxide prepared by different chemical oxidation methods. *Ceram. Int.* **2019**, *45*, 14439−14448.
(32) Du, C.; Yan, B.; Lin, Z.; Yang, G. Cross-linked bond accelerated interfacial charge transfer in monolayer zinc indium sulfide ($ZnIn_2S_4$)/reduced graphene oxide (RGO) heterostructure for photocatalytic hydrogen production with mechanistic insight. *Catal. Sci. Technol.* **2019**, *9*, 4066−4076.
(33) Ito, Y.; Cong, W.; Fujita, T.; Tang, Z.; Chen, M. High catalytic activity of nitrogen and sulfur co-doped nanoporous graphene in the hydrogen evolution reaction. *Angew. Chem. Int. Ed.* **2015**, *54*, 2131−6.
(34) Wang, H.; Maiyalagan, T.; Wang, X. Review on recent progress in nitrogen-doped graphene: synthesis, characterization, and its potential applications. *ACS catal.* **2012**, *2*, 781−794.
(35) Wang, Y.; Chen, D.; Qin, L.; Liang, J.; Huang, Y. Hydrogenated $ZnIn_2S_4$ microspheres: boosting photocatalytic hydrogen evolution by

https://doi.org/10.1021/jacsau.3c00482
JACS Au 2023, 3, 3127−3140

sulfur vacancy engineering and mechanism insight. *Phys. Chem. Chem. Phys.* **2019**, *21*, 25484−25494.
(36) Ma, Y.; Hai, G.; Atinafu, D. G.; Dong, W.; Li, R.; Hou, C.; Wang, G. Carbon inserted defect-rich MoS_{2-X} nanosheets@CdS nanospheres for efficient photocatalytic hydrogen evolution under visible light irradiation. *J. Colloid Interface Sci.* **2020**, *569*, 89−100.
(37) Chen, X.; Yin, H.; Yang, X.; Zhang, W.; Xiao, D.; Lu, Z.; Zhang, Y.; Zhang, P. Co-doped Fe_3S_4 nanoflowers for boosting electrocatalytic nitrogen fixation to ammonia under mild conditions. *Inorg. Chem.* **2022**, *61*, 20123−20132.
(38) Zhang, S.; Liu, X.; Liu, C.; Luo, S.; Wang, L.; Cai, T.; Zeng, Y.; Yuan, J.; Dong, W.; Pei, Y.; et al. MoS_2 quantum dot growth induced by S vacancies in a $ZnIn_2S_4$ monolayer: atomic-level heterostructure for photocatalytic hydrogen production. *ACS Nano* **2018**, *12*, 751−758.
(39) Jiao, X.; Chen, Z.; Li, X.; Sun, Y.; Gao, S.; Yan, W.; Wang, C.; Zhang, Q.; Lin, Y.; Luo, Y.; et al. Defect-mediated electron-hole separation in one-unit-cell $ZnIn_2S_4$ layers for boosted solar-driven CO_2 reduction. *J. Am. Chem. Soc.* **2017**, *139*, 7586−7594.
(40) Guan, Z.; Wang, P.; Li, Q.; Li, G.; Yang, J. Constructing a $ZnIn_2S_4$ nanoparticle/MoS_2-RGO nanosheet 0D/2D heterojunction for significantly enhanced visible-light photocatalytic H_2 production. *Dalton Trans.* **2018**, *47*, 6800−6807.
(41) Murphy, A. B. Band-gap determination from diffuse reflectance measurements of semiconductor films, and application to photoelectrochemical water-splitting. *Sol. Energy Mater. Sol. Cells.* **2007**, *91*, 1326−1337.
(42) Zhang, H.; Zhang, P.; Qiu, M.; Dong, J.; Zhang, Y.; Lou, X. W. Ultrasmall MoO_x clusters as a novel cocatalyst for photocatalytic hydrogen evolution. *Adv. Mater.* **2019**, *31*, 1804883.
(43) Godin, R.; Wang, Y.; Zwijnenburg, M. A.; Tang, J.; Durrant, J. R. Time-resolved spectroscopic investigation of charge trapping in carbon nitrides photocatalysts for hydrogen generation. *J. Am. Chem. Soc.* **2017**, *139*, 5216−5224.
(44) Wu, K.; Liang, G.; Shang, Q.; Ren, Y.; Kong, D.; Lian, T. Ultrafast interfacial electron and hole transfer from $CsPbBr_3$ perovskite quantum dots. *J. Am. Chem. Soc.* **2015**, *137*, 12792−12795.
(45) Jiang, Y.; Chen, H.; Li, J.; Liao, J.; Zhang, H.; Wang, X.; Kuang, D. Z-scheme 2D/2D heterojunction of $CsPbBr_3/Bi_2WO_6$ for improved photocatalytic CO_2 reduction. *Adv. Funct. Mater.* **2020**, *30*, 2004293.
(46) Wu, B.; Zhang, L.; Jiang, B.; Li, Q.; Tian, C.; Xie, Y.; Li, W.; Fu, H. Ultrathin porous carbon nitride bundles with an adjustable energy band structure toward simultaneous solar photocatalytic water splitting and selective phenylcarbinol oxidation. *Angew. Chem., Int. Ed.* **2021**, *60*, 4815−4822.
(47) Tian, L.; Xie, W.; Wu, X.; Guo, B.; Xie, G.; Cheng, P.; Liu, X.; Gong, J. R. Overall regulation of exciton dynamics by defect engineering in polymeric photocatalysts for hydrogen evolution. *J. Phys. Chem. C* **2020**, *124*, 24667−24676.
(48) Peng, H.; Yang, T.; Lin, H.; Xu, Y.; Wang, Z.; Zhang, Q.; Liu, S.; Geng, H.; Gu, L.; Wang, C.; et al. Ru/In dual-Single atoms modulated charge separation for significantly accelerated photocatalytic H_2 evolution in pure water. *Adv. Energy Mater.* **2022**, *12*, 2201688.
(49) Lu, H.; Ran, G.; Liu, Y.; Pei, Z.; Liu, W.; Liu, Y.; Tang, Z.; Zhang, W.; Bo, Z. Green-solvent-processed high-performance ternary organic solar cells comprising a highly soluble and fluorescent third component. *Adv. Funct. Mater.* **2023**, *33*, 2301866.
(50) Wang, W.; Bai, X.; Ci, Q.; Du, L.; Ren, X.; Phillips, D. L. Near-field drives long-lived shallow trapping of polymeric C_3N_4 for efficient photocatalytic hydrogen evolution. *Adv. Funct. Mater.* **2021**, *31*, 2103978.
(51) Liu, X.; Zhang, Q.; Zhao, S.; Wang, Z.; Liu, Y.; Zheng, Z.; Cheng, H.; Dai, Y.; Huang, B.; Wang, P. Integrating mixed halide perovskite photocatalytic HI splitting and electrocatalysis into a loop for efficient and robust pure water splitting. *Adv. Mater.* **2023**, *35*, 2208915.
(52) Sun, Q. M.; Xu, J. J.; Tao, F. F.; Ye, W.; Zhou, C.; He, J. H.; Lu, J. M. Boosted inner surface charge transfer in perovskite nanodots@mesoporous titania frameworks for efficient and selective photocatalytic CO_2 reduction to methane. *Angew. Chem., Int. Ed.* **2022**, *61*, No. e202200872.
(53) Khan, M.; Maity, P.; Al-Oufi, M.; Al-Howaish, I.; Idriss, H. Electron transfer of the metal/semiconductor system in photocatalysis. *J. Phys. Chem. C* **2018**, *122*, 16779−16787.
(54) Tong, X.; Shou, J.; Song, H.; Wang, Y.; Huang, L.; Yin, L. Ultrafast electron transfer from crystalline g-C_3N_4 to Pt revealed by femtosecond transient absorption spectroscopy. *Energy Fuel.* **2022**, *36*, 11532−11541.
(55) Wang, W.; Tao, Y.; Du, L.; Wei, Z.; Yan, Z.; Chan, W. K.; Lian, Z.; Zhu, R.; Phillips, D. L.; Li, G. Femtosecond time-resolved spectroscopic observation of long-lived charge separation in bimetallic sulfide/g-C_3N_4 for boosting photocatalytic H_2 evolution. *Appl. Catal. B: Environ.* **2021**, *282*, 119568.
(56) Xue, J.; Fujitsuka, M.; Majima, T. Shallow trap state-induced efficient electron transfer at the interface of heterojunction photocatalysts: the crucial role of vacancy defects. *ACS Appl. Mater. Interfaces* **2019**, *11*, 40860−40867.
(57) Wang, W.; Bai, X.; Ci, Q.; Du, L.; Ren, X.; Phillips, D. L. Near-field drives long-lived shallow trapping of polymeric C_3N_4 for efficient photocatalytic hydrogen evolution. *Adv. Funct. Mater.* **2021**, *31*, 2103978.
(58) Huang, W. H.; Su, C. Y.; Zhu, C.; Bo, T. T.; Zuo, S. W.; Zhou, W.; Ren, Y. F.; Zhang, Y. A.; Zhang, J.; Rueping, M.; Zhang, H. B. Isolated electron trap-induced charge accumulation for efficient photocatalytic hydrogen production. *Angew. Chem., Int. Ed.* **2023**, *62*, e202304634.
(59) Xi, Q.; Xie, F.; Liu, J.; Zhang, X.; Wang, J.; Wang, Y.; Wang, Y.; Li, H.; Yu, Z.; Sun, Z.; et al. In situ formation $ZnIn_2S_4/Mo_2TiC_2$ Schottky junction for accelerating photocatalytic hydrogen evolution kinetics: manipulation of local coordination and electronic structure. *Small.* **2023**, *19*, 2300717.
(60) Tang, T.; Ding, L.; Yao, Z. C.; Pan, H. R.; Hu, J. S.; Wan, L. J. Synergistic electrocatalysts for alkaline hydrogen oxidation and evolution reactions. *Adv. Funct. Mater.* **2022**, *32*, 2107479.
(61) Chen, R.; Ren, Z.; Liang, Y.; Zhang, G.; Dittrich, T.; Liu, R.; Liu, Y.; Zhao, Y.; Pang, S.; An, H.; Ni, C.; Zhou, P.; Han, K.; Fan, F.; Li, C. Spatiotemporal imaging of charge transfer in photocatalyst particles. *Nature.* **2022**, *610*, 296−301.
(62) O'Regan, B. C.; Bakker, K.; Kroeze, J.; Smit, H.; Sommeling, P.; Durrant, J. R. Measuring charge transport from transient photovoltage rise times. a new tool to investigate electron transport in nanoparticle films. *J. Phys. Chem. B* **2006**, *110*, 17155−17160.
(63) Li, C. Q.; Du, X.; Jiang, S.; Liu, Y.; Niu, Z. L.; Liu, Z. Y.; Yi, S. S.; Yue, X. Z. Constructing direct Z-scheme heterostructure by enwrapping $ZnIn_2S_4$ on CdS hollow cube for efficient photocatalytic H_2 generation. *Adv. Sci.* **2022**, *9*, 2201773.
(64) Ran, J.; Zhang, H.; Fu, S.; Jaroniec, M.; Shan, J.; Xia, B.; Qu, Y.; Qu, J.; Chen, S.; Song, L.; Cairney, J. M.; Jing, L.; Qiao, S.-Z. $NiPS_3$ ultrathin nanosheets as versatile platform advancing highly active photocatalytic H_2 production. *Nat. Commun.* **2022**, *13*, 4600.
(65) Lai, H.; Lu, Z.; Lu, Y.; Yao, X.; Xu, X.; Chen, J.; Zhou, Y.; Liu, P.; Shi, T.; Wang, X.; et al. Fast, multi-bit, and vis-infrared broadband nonvolatile optoelectronic memory with MoS_2/2D-perovskite van der waals heterojunction. *Adv. Mater.* **2023**, *35*, 2208664.
(66) Hua, C.; Zhou, S.; Zhou, C.; Dou, W.; Li, H.; Lu, Y.; Zhong, J.; Mao, H. Work function modulation of graphene with binary mixture of Cu and $C_{60}F_{36}$. *Carbon.* **2021**, *179*, 172−179.
(67) Du, C.; Yan, B.; Lin, Z.; Yang, G. Enhanced carrier separation and increased electron density in 2D heavily N-doped $ZnIn_2S_4$ for photocatalytic hydrogen production. *J. Mater. Chem. A* **2020**, *8*, 207−217.
(68) Jin, Z.; Li, H.; Li, J. Efficient photocatalytic hydrogen evolution over graphdiyne boosted with a cobalt sulfide formed S-scheme heterojunction. *Chin. J. Catal.* **2022**, *43*, 303−315.

https://doi.org/10.1021/jacsau.3c00482
JACS Au 2023, 3, 3127−3140

(69) Ravishankar, S.; Bisquert, J.; Kirchartz, T. Interpretation of Mott−Schottky plots of photoanodes for water splitting. *Chem. Sci.* **2022**, *13*, 4828−4837.
(70) Chu, X.; Ye, Q.; Wang, Z.; Zhang, C.; Ma, F.; Qu, Z.; Zhao, Y.; Yin, Z.; Deng, H.-X.; Zhang, X.; You, J. Surface in situ reconstruction of inorganic perovskite films enabling long carrier lifetimes and solar cells with 21% efficiency. *Nat. Energy.* **2023**, *8*, 372−380.

https://doi.org/10.1021/jacsau.3c00482
JACS Au 2023, 3, 3127−3140